December 1991

M 91-114

J. Providakes
T. J. Elkins
R. B. Godwin
M. C. Kelley

ESD/RADC OTH RADAR SYMPOSIUM, 5–7 NOVEMBER 1991, HANSCOM AFB

AN OTH RADAR CLUTTER SIMULATION

"Original contains color plates: All DTIC reproductions will be in black and white"

MITRE
Bedford, Massachusetts

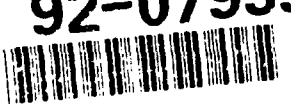

DISCLAIMER NOTICE

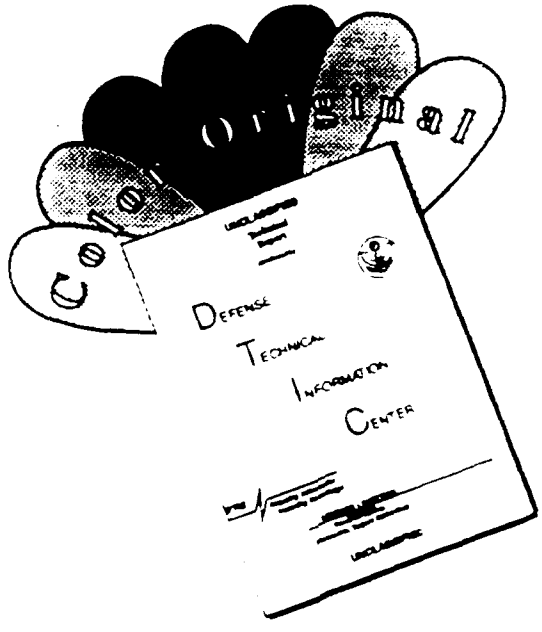

THIS DOCUMENT IS BEST QUALITY AVAILABLE. THE COPY FURNISHED TO DTIC CONTAINED A SIGNIFICANT NUMBER OF COLOR PAGES WHICH DO NOT REPRODUCE LEGIBLY ON BLACK AND WHITE MICROFICHE.

December 1991

M 91-114

J. Providakes
T. J. Elkins
R. B. Godwin
M. C. Kelley

ESD/RADC OTH
RADAR SYMPOSIUM,
5–7 NOVEMBER 1991,
HANSCOM AFB

AN OTH RADAR CLUTTER SIMULATION

CONTRACT SPONSOR ESD
CONTRACT NO. F19628-89-C-0001
PROJECT NO. 41411
DEPT. D085

MITRE

The MITRE Corporation
Bedford, Massachusetts

ABSTRACT

A computer simulation is described which was developed with the objective of arriving at an understanding of OTH radar clutter originating in the equatorial ionosphere. This source of clutter is of particular interest in OTH radar, since all radar propagation paths must pass through the equatorial region, even if the desired targets are far removed from it. A central feature of the simulation is an ionospheric propagation model developed to synthesize OTH radar clutter by making use of state-of-the art models for global ionospheric structure, including small-scale irregularities, and combining these with efficient ray tracing procedures and a multiple phase-screen approach to computing the diffraction of radar energy by the irregular ionosphere. Simulated clutter data is compared to actual measurements using several radars, with generally satisfactory results.

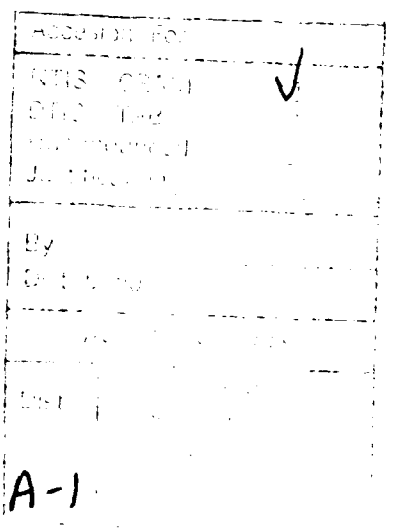

ESD/RADC OTH RADAR SYMPOSIUM
5-7 NOVEMBER 1991
HANSCOM AFB

AN OTH RADAR CLUTTER SIMULATION

J. Providakes
T. J. Elkins
R. B. Godwin

The MITRE Corporation
Bedford, MA 01730

M. C. Kelley

Cornell University
School of Electrical Engineering
Ithaca, NY 14853

1. INTRODUCTION

The term Over-the-Horizon (OTH) radar clutter is used to characterize unwanted signals above the normal high-frequency (HF) background noise level that may obscure targets. The generation of OTH radar clutter involves complex processes associated with HF energy propagation through a structured ionosphere and scattering from the earth's surface. Global ionospheric "weather" patterns generate ionospheric plasma irregularities ranging from planetary scales (several thousand kilometers) down to small scales (less than a meter). The complex interaction of HF energy with these irregularities, via transmission, reflection, and scattering processes, appears to be a principal source of performance degradation of OTH radar clutter as well as HF communication systems. The propagation of an HF radio-wave signal through turbulent large-scale ionospheric structures will induce signal delay and Doppler spread, as will backward and forward scattering from small- and intermediate-scale ionospheric irregularities. A primary source of clutter for current OTH radars is equatorial spread F (highly structured ionospheric density and velocity fields near the earth's magnetic equator). Because of radar waveform ambiguity in measuring the range of very distant targets, radar returns from this region appear to arrive at the normal radar target detection ranges. For advanced OTH

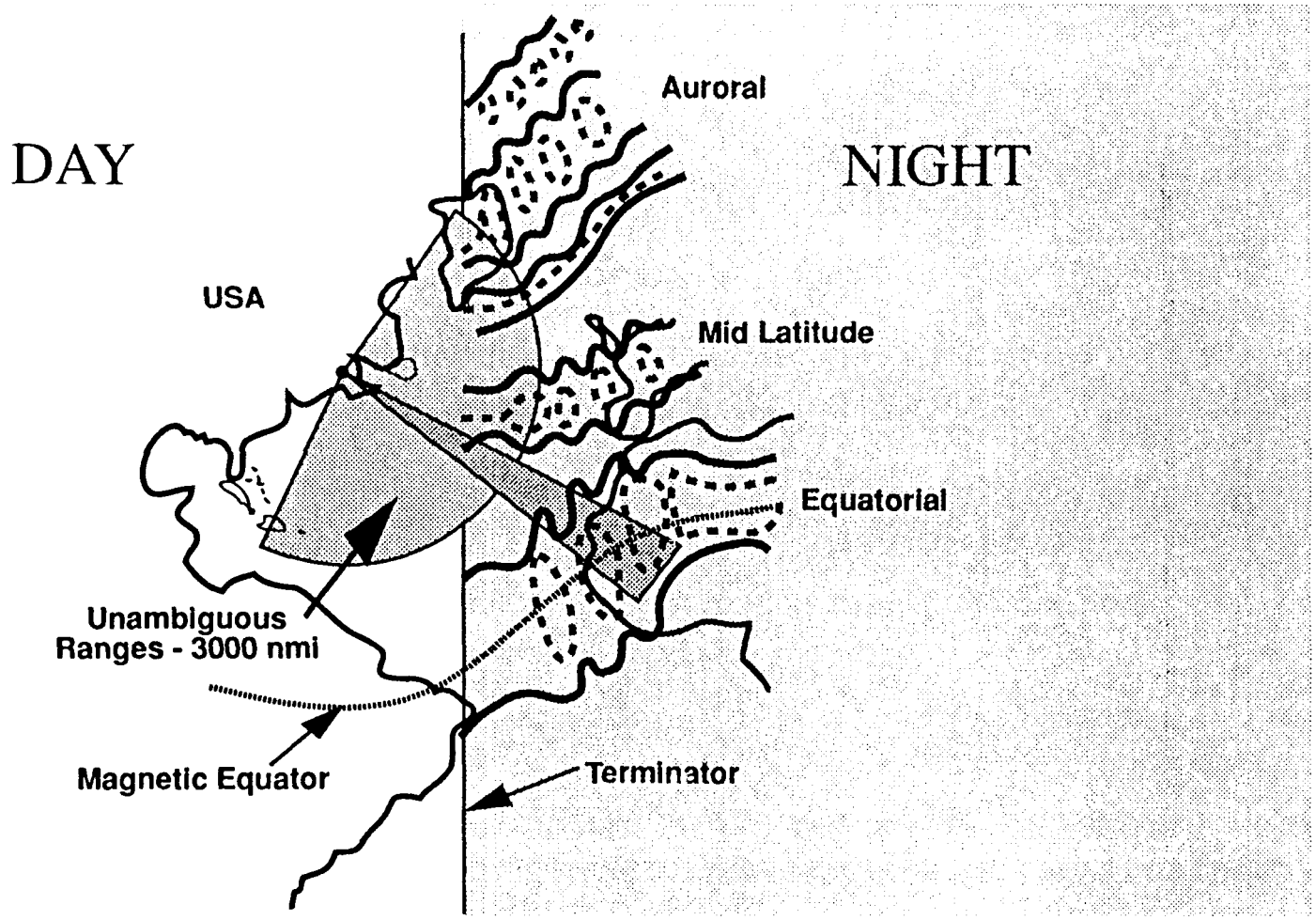

Figure 1. Ionospheric Structure Exists on a Global Scale

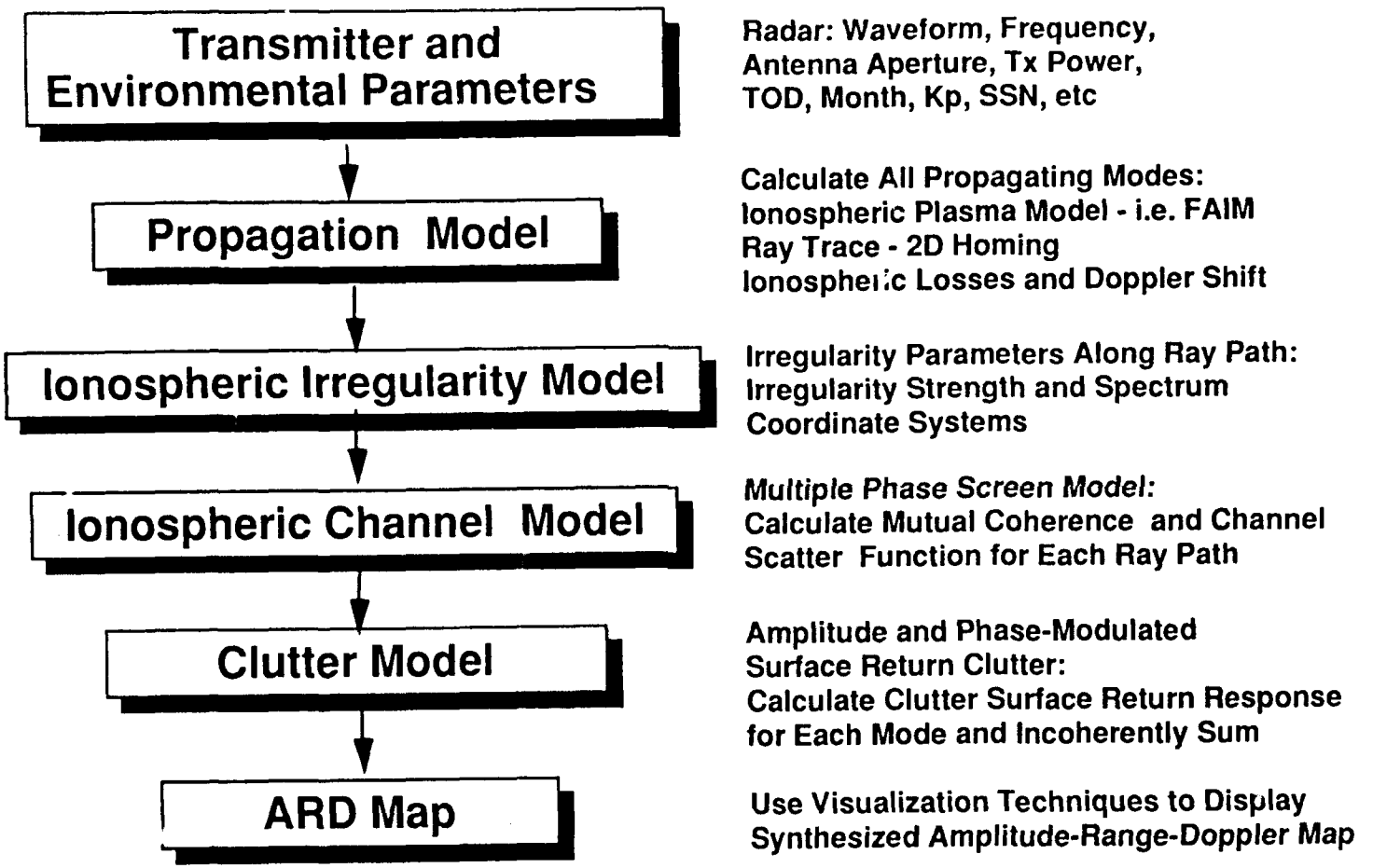

Figure 2. Overview of Ionospheric Propagation Simulation: OTH Radar Clutter

Time =00 UT; SSN = 87

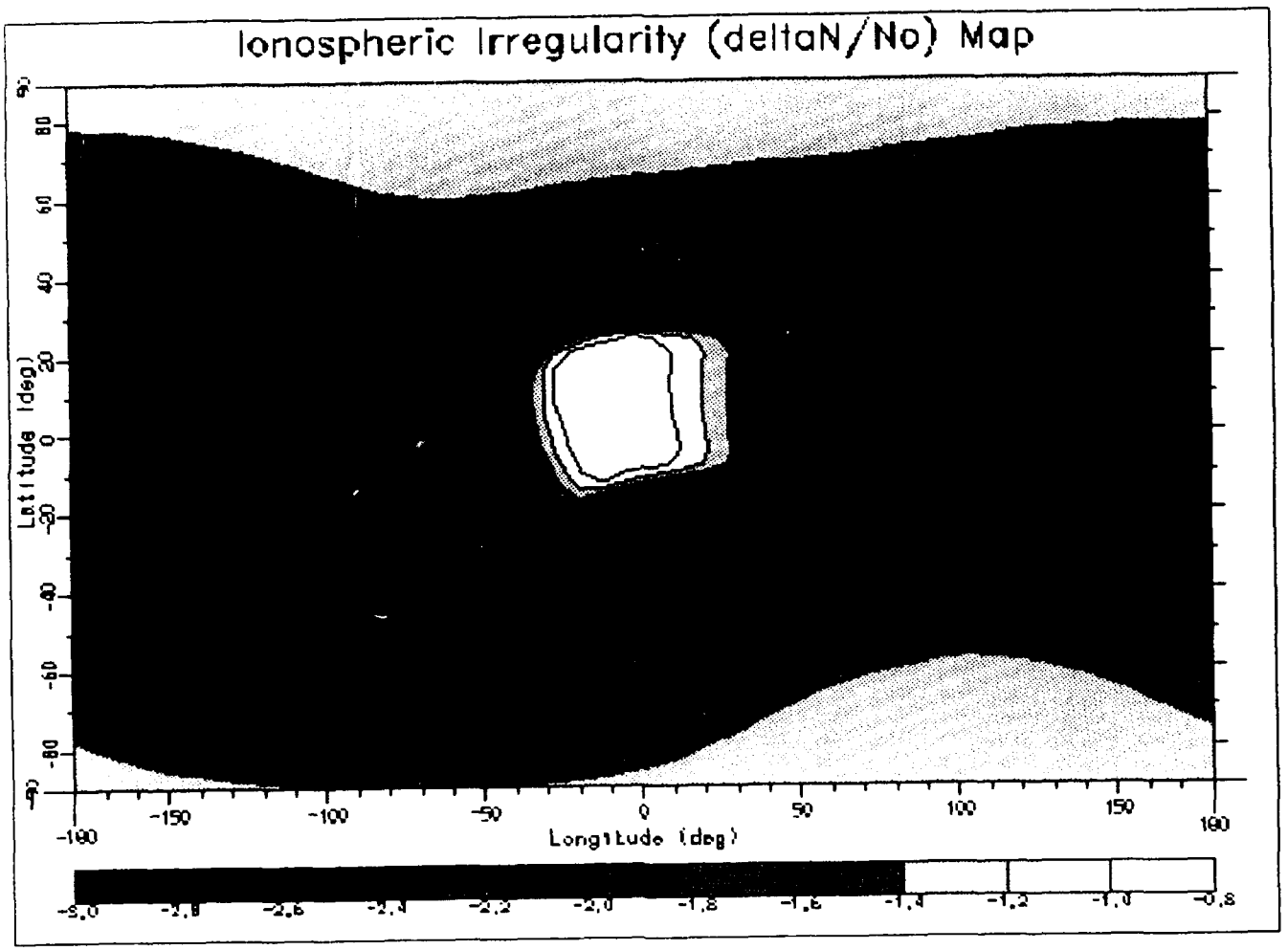

Figure 3. Contours of Ionospheric Irregularity Fluctuations Obtained from WBMOD for a Constant Altitude of 350 km as a Function of Latitude and Longitude

As part of the channel model, for each ray path or propagation mode we calculate the group path length (for a specified slant or ground range); the ionospheric propagation path loss (D-region absorption and $1/R^3$ spreading loss); and the Doppler shift due to vertical motion of the ionosphere, as well as the irregularity amplitudes and associated transverse plasma drift velocity. For each mode we also calculate multipath fading caused by the presence of irregularities in the ionosphere. We have neglected fading associated with interference between different modes of propagation (i.e., multiple modes, O- and X-modes, high-angle and low-angle rays, etc.) as well as dispersion. Dispersion can be straightforwardly calculated, but for narrowband radars it is negligible. Multi-mode interference is more complicated because it must take refractive effects into account. Future work of this study will include multi-mode interference.

The number of screens necessary for approximating the extended (turbulent) medium along a given ray path depends on the thickness of the turbulent region that the ray traverses as well as on the size of the transverse velocity shear in the direction of propagation. We are interested in simulating clutter originating from spread-Doppler surface backscatter, which is associated with equatorial spread F. We found that three phase screens placed appropriately are sufficient to capture most of the channel scattering function shape. More phase screens could have been used, but we must trade off numerical computation time for greater accuracy in the shape of the channel scattering function. The phase screens were placed along the ray path in the general region of greatest irregularity intensity, with the first one placed at the location of greatest irregularity intensity. The other two phase screens were placed on either side of the first phase screen at the locations where the irregularity amplitude falls off to one-half of its peak value. The effective screen thickness is given by the distance between adjacent phase screens. The transverse horizontal velocity is computed at the location of each screen.

Figure 4 shows a global view of the situation, with a propagation mode passing through regions of strong ionospheric irregularities. The strengths of the irregularities, obtained using WBMOD, are plotted by deforming a surface above the globe at regions of high ionospheric irregularities. Note the bulges at both poles and the rather prominent bulge centered on the magnetic equator and the terminator (not shown). The four-hop mode passes through the equatorial zone where strong irregularities are present. The placement positions of three phase

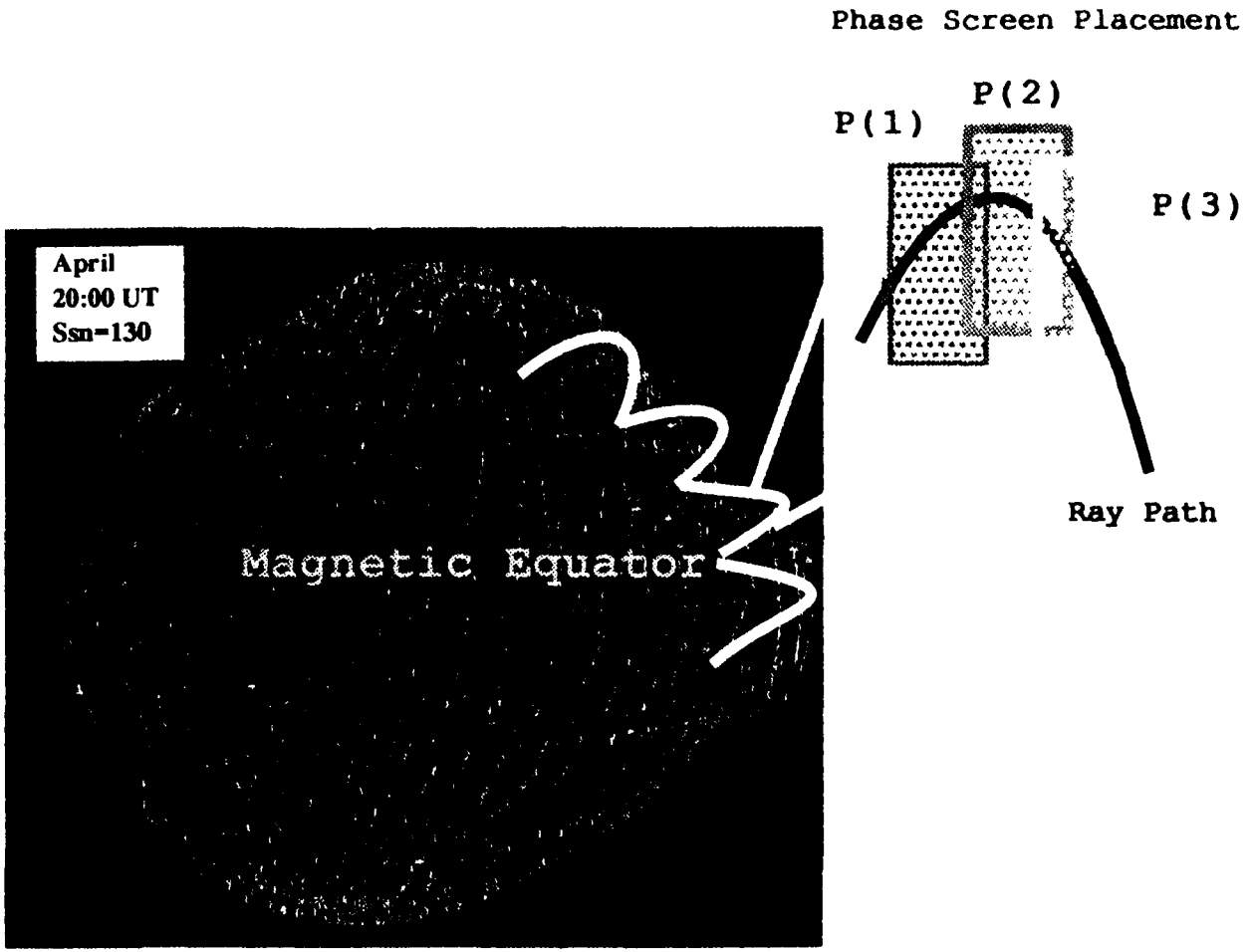

Figure 4. Propagation Mode Passing through Regions of Strong Irregularities

screens are also shown. They were placed by the program near the peak of the third hop. The fourth hop is actually deeper into the irregularity "bulge," but this portion of the ray path is located in a region of low electron density; thus the scintillation contribution is small. Maximum scintillation effects occur on the third hop portion.

Figure 5 shows an example of one unambiguous mode (2000 km) and two ambiguous modes for propagation paths originating from the East Coast Radar System (ECRS) at an azimuth of 110 degrees east and a fixed frequency of 13 MHz. Shown are contours of electron density generated from FAIM. The electron density contours show the classical equatorial anomaly centered about the magnetic equator at a ground range of about 5000 km. The ionospheric irregularity amplitude (δn) is depicted along the ray paths as a color-modulated display with red = low and white = high. Note that the irregularities are most intense along the ray path on the southern side of the magnetic equator where the rays penetrate most deeply into the ionosphere (i.e., reaching altitudes where $<n_e>$ and $<\delta n_e^2>$ are greater).

In summary, the ionospheric HF channel model includes determining all propagation modes; calculating the two-position, two-frequency, two-time mutual coherence function for each one-way path mode; computing the received signal response at the output of the antenna for each mode; and incoherently summing the received signals on all modes. Future studies will include taking into account interference between different modes of propagation (i.e., O- and X-modes).

3. SIMULATION RESULTS

Figure 6 shows the mutual coherence function $\Gamma(\Delta f, \Delta t, \Delta x=0, \Delta y=0.0)$, and the scattering function (2-D Fourier transform of Γ) $S(\tau, f)$ as predicted by our model for a disturbed transequatorial ionospheric propagation path. The transmitter is located at the ECRS site and is directed at an azimuth of 110.0 degrees. The calculation is for the month of April at 20:00 hours universal time and for high sunspot activity (sunspot number 130). This case was chosen, of course, to coincide with data we have available from the ECRS, but the results are

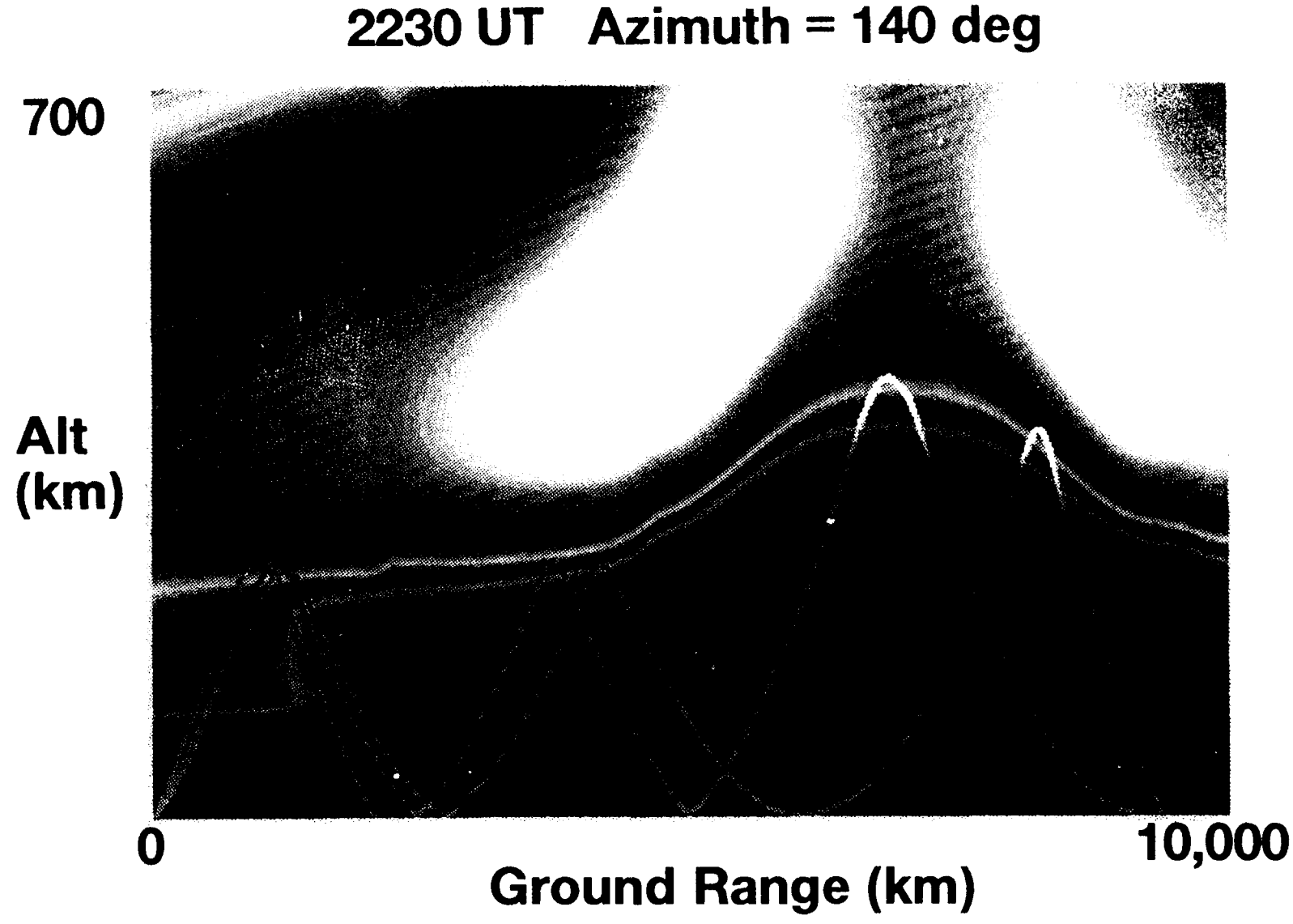

Figure 5. Example of One Unambiguous (2,000 km) Mode and Two Ambiguous Modes from the ECRS

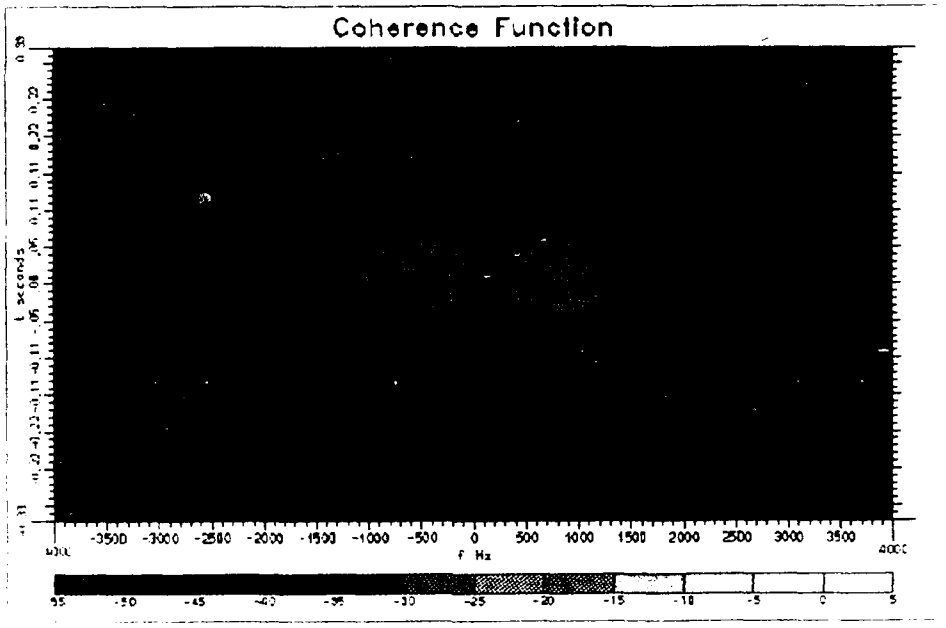

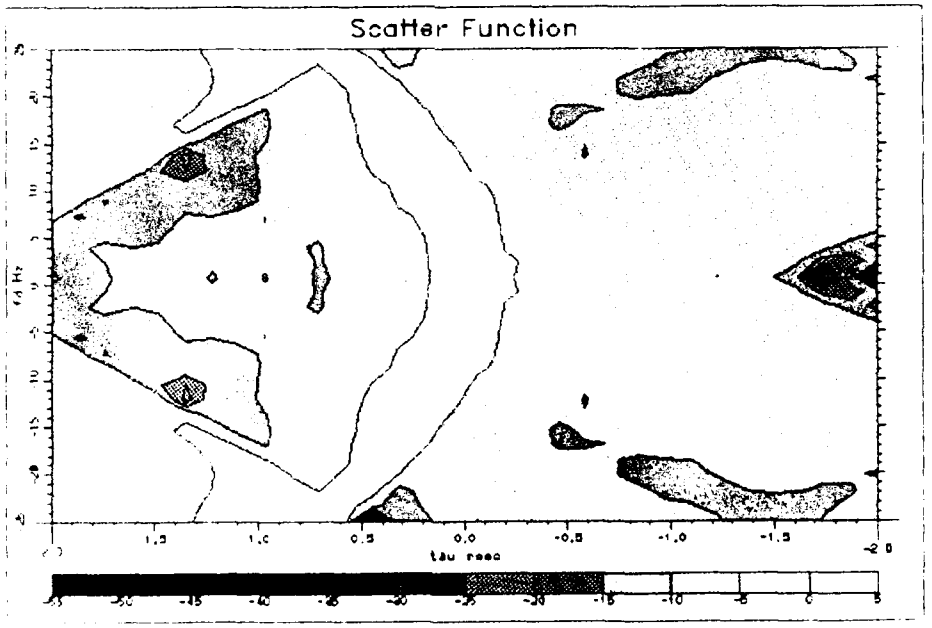

Figure 6. Coherence and Scatter Function for a Transequatorial Ionospheric Path as Predicted by the Simulation (Path is Shown in Figure 4)

also of interest to HF communications at low to mid-latitudes. Contours are plotted in dBs. Note that the coherence bandwidth of this mode is fairly small, on the order of 500 Hz. Decorrelation time is also small, about 20 msec. Note the characteristic "wing-like" structure of the scatter function, as a function of delay and Doppler spread, which is a result of the correlation between these two parameters brought about by the scattering geometry. The scatter function shows a corresponding delay spread of about 2 msec and Doppler spread of 70 Hz. Here we use the 5-dB point as a measure of spread simply because it is easily read from the intensity plots.

Figure 7 shows the effect of decreasing the screen velocities by a factor of two and the strength of the irregularities (defined as the rms value of $\Delta n/n_e$) by 0.1. The result is a decrease in Doppler spread by about a factor of two, as expected, indicated by the compression of the wing structure of $S(\tau,f)$ in Doppler. Figure 8 shows the result of both decreasing the screen velocities by two and applying an increased shear of one screen relative to the next, by moving the screens in opposite directions. This shear could be caused by turbulence in the medium; here we simply increase it to see its effect on the channel's coherence and scatter functions. From the figure we see that with this increased shear the coherence function becomes narrowed in Δt with increasing Δf. The coherence bandwidth and coherence time remain very close to the model, with small shear and identical screen velocities. A comparison of the scatter functions for the two cases shows a pronounced change in shape. We observe a marked change in the distribution of scattered energy as a function of time-delay and Doppler frequency. The scatter function's wing structure becomes filled in, implying an increased decorrelation of scattered energy with Doppler shift. Physically, this is possible in a multiple phase-screen formulation because although a scattered radio-wave signal with a fixed time-delay, for example, may gain some Doppler shift as it propagates through one screen, it may lose that Doppler shift as it passes through the second screen which is moving in the opposite direction. Hence, small Doppler shifts may be exhibited at large time-delays, which smears out the wing structure.

As we mentioned earlier, the clutter model is based on using multiple phase screens to model diffractive scattering of HF energy by small-scale ionospheric irregularities. From an OTH radar application viewpoint, this multiple diffractive scattering of the signal creates phase

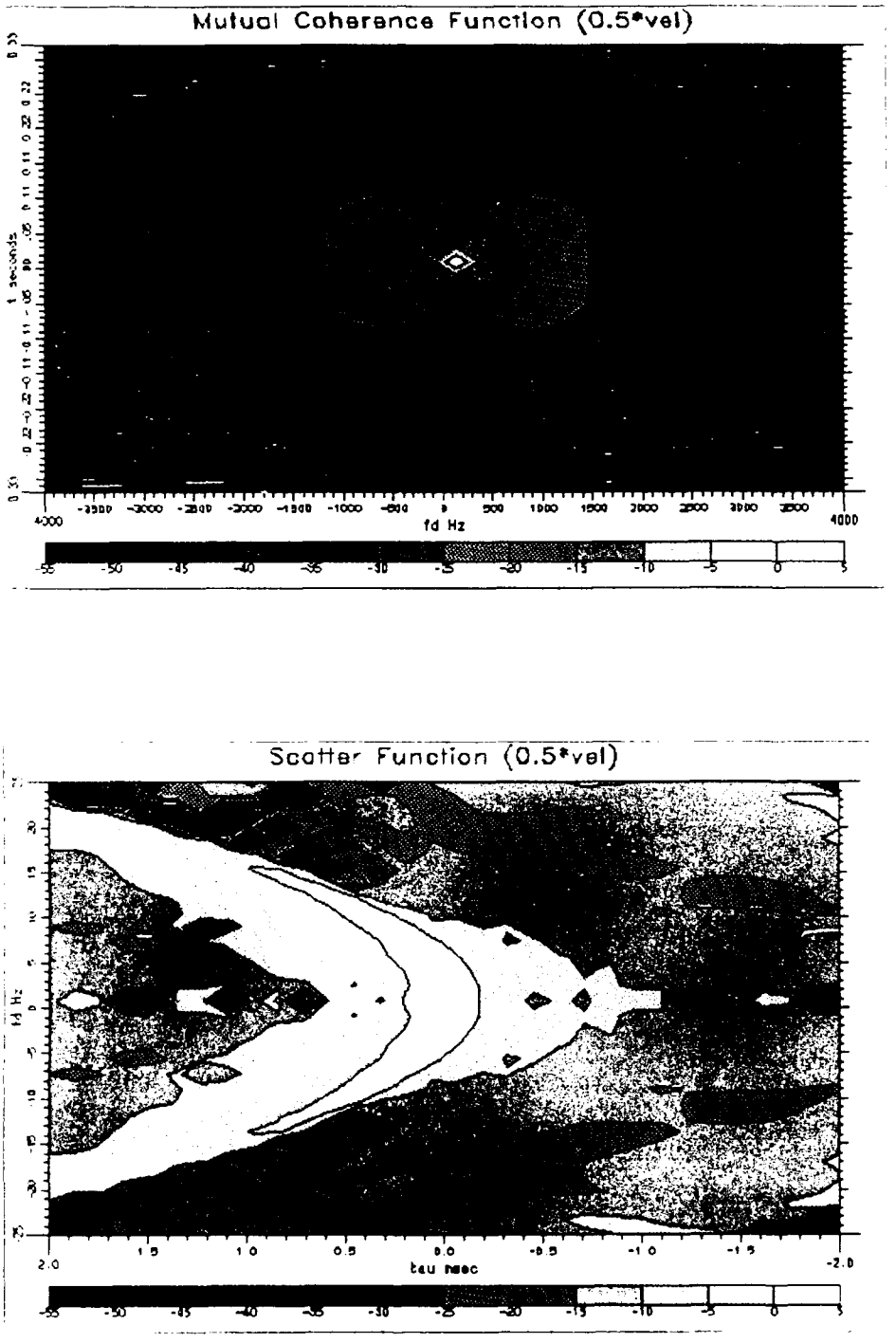

Figure 7. Coherence and Scatter Function for a Transequatorial Ionospheric Path as Predicted by the Simulation, Except the Transverse Velocity is Reduced by 0.5 (the Path is Shown in Figure 4)

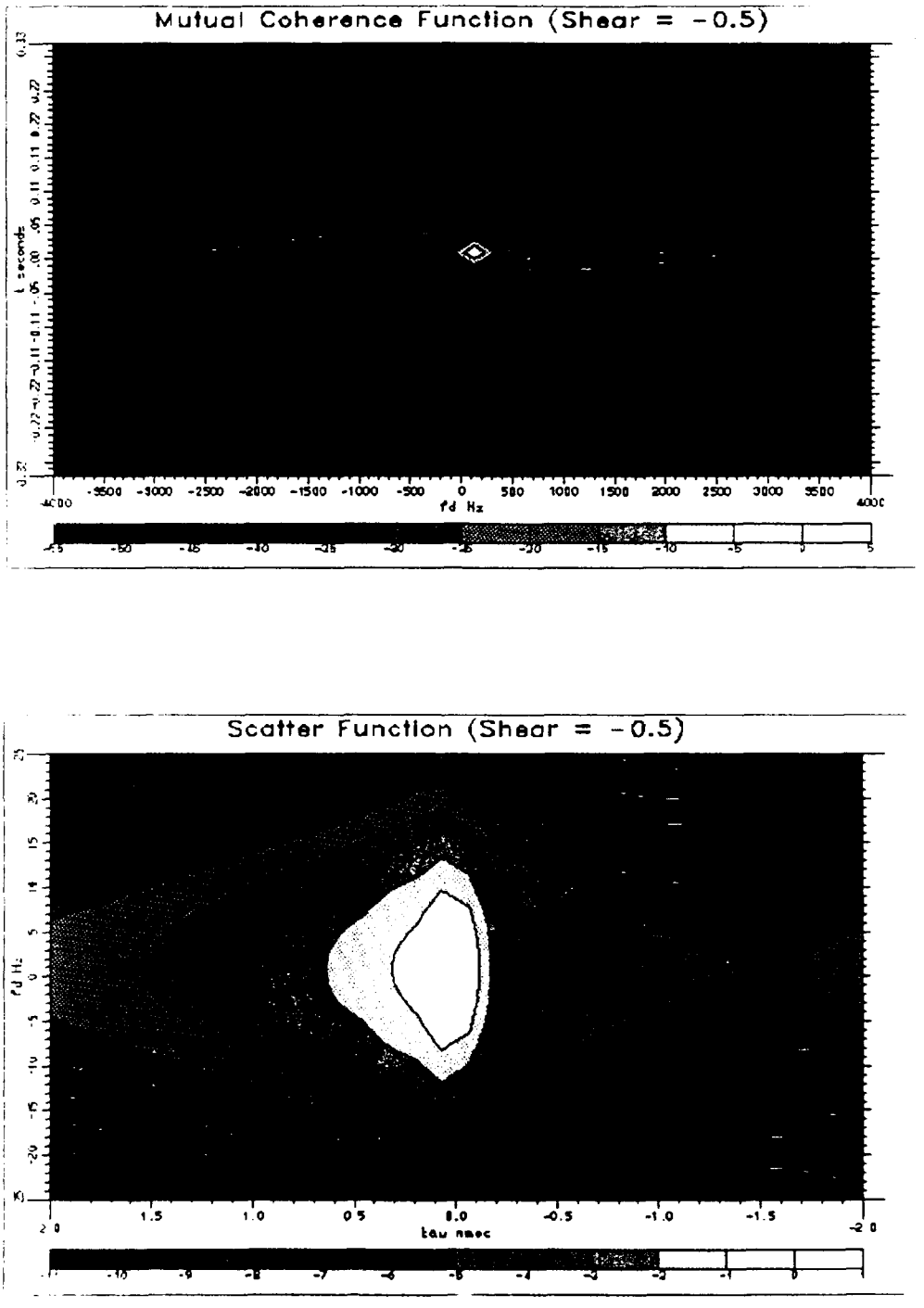

Figure 8. Coherence and Scatter Function for a Transequatorial Ionospheric Path as Predicted by the Simulation

- Numerically compute channel scatter function for all propagation paths at fixed slant range (including ambiguous ranges)
- Incoherently sum all scattered signal responses for all modes

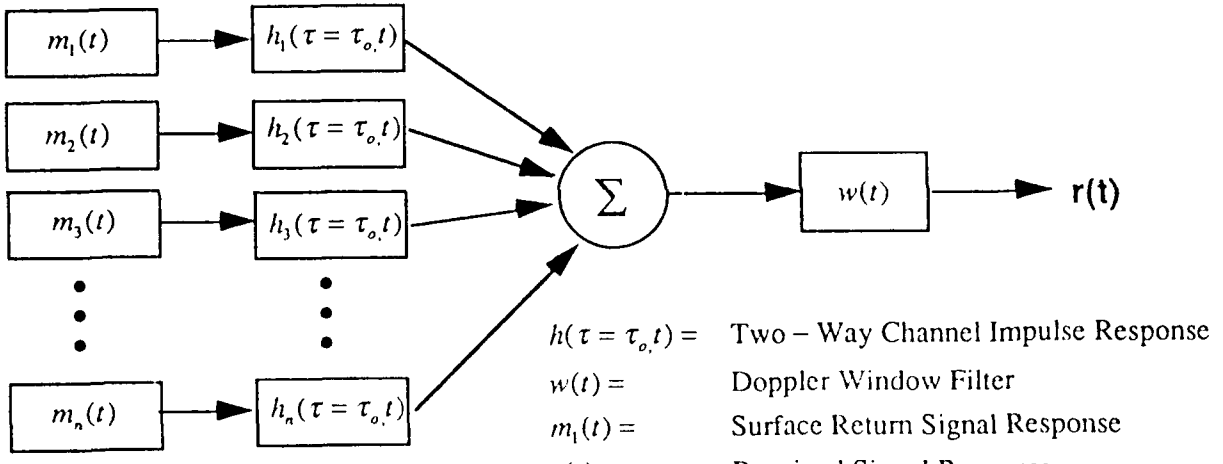

Figure 9. Spread-Doppler Surface Return Clutter Model

environmental parameters are specified, all possible unambiguous and ambiguous range propagation paths are determined for a fixed transmitter location.

Figure 10 shows both measured and simulated radar Doppler power spectra data. The measured data correspond to ECRS range-folded clutter data. The simulated data correspond to the same time period (20 UT), radar operating frequency (21 MHz), coherent integration time (CIT = 12 seconds), waveform repetition frequency (WRF = 20 Hz), azimuth (110°), range-start, and range-extent. An SSN of 130 was used with a Kp = 2.0. The average transverse velocity for the phase screens was about 300 m/s, and the average ionospheric irregularity fluctuation level was about 0.3. A multiplier of 1.2 was applied to the modeled first hop foF2 values to maintain the one-hop ground coverage between 2000 and 3000 km as observed by the radar under these conditions. Appropriate radar transmitter power, antenna gain, losses, etc., were applied to the simulated data, as well as a sampling of 128 Doppler cells. Both the unambiguous one-hop surface response and the range-folded equatorial clutter are evident in the simulated and measured data. The general spectral shape and Doppler shift of the range-folded clutter are in good agreement. The sea Bragg lines are also clearly resolved in both the measured and simulated data. Note that an HF background noise component and a statistical random signal component (i.e., a Rayleigh distribution with a variance dependent on the number of samples) have been added to the simulated data for cosmetic purposes. We could easily have smoothed the measured data and then compared it with the simulated data.

Figure 11 shows both measured and simulated 2-D Nested-Range-Doppler data using a sampling of 32 range gates. The similarity between the simulated and measured ECRS data is clearly evident. Figure 12 shows the same measured and simulated data given in figure 11, but displays it in a 2-D color-modulated format. The different color steps correspond to 10-dB increments. The overall good agreement between measurement and simulation of the spectral shape and Doppler shift is displayed. Again, the sea Bragg lines are evident in the unambiguous surface return response in both the simulated and measured data.

To begin investigating the general validity of the simulation, we compared simulation results to measured data for two different azimuths. Figure 12 corresponds to a comparison made at a radar azimuth of 110 degrees, while figure 13 compares simulated and measured

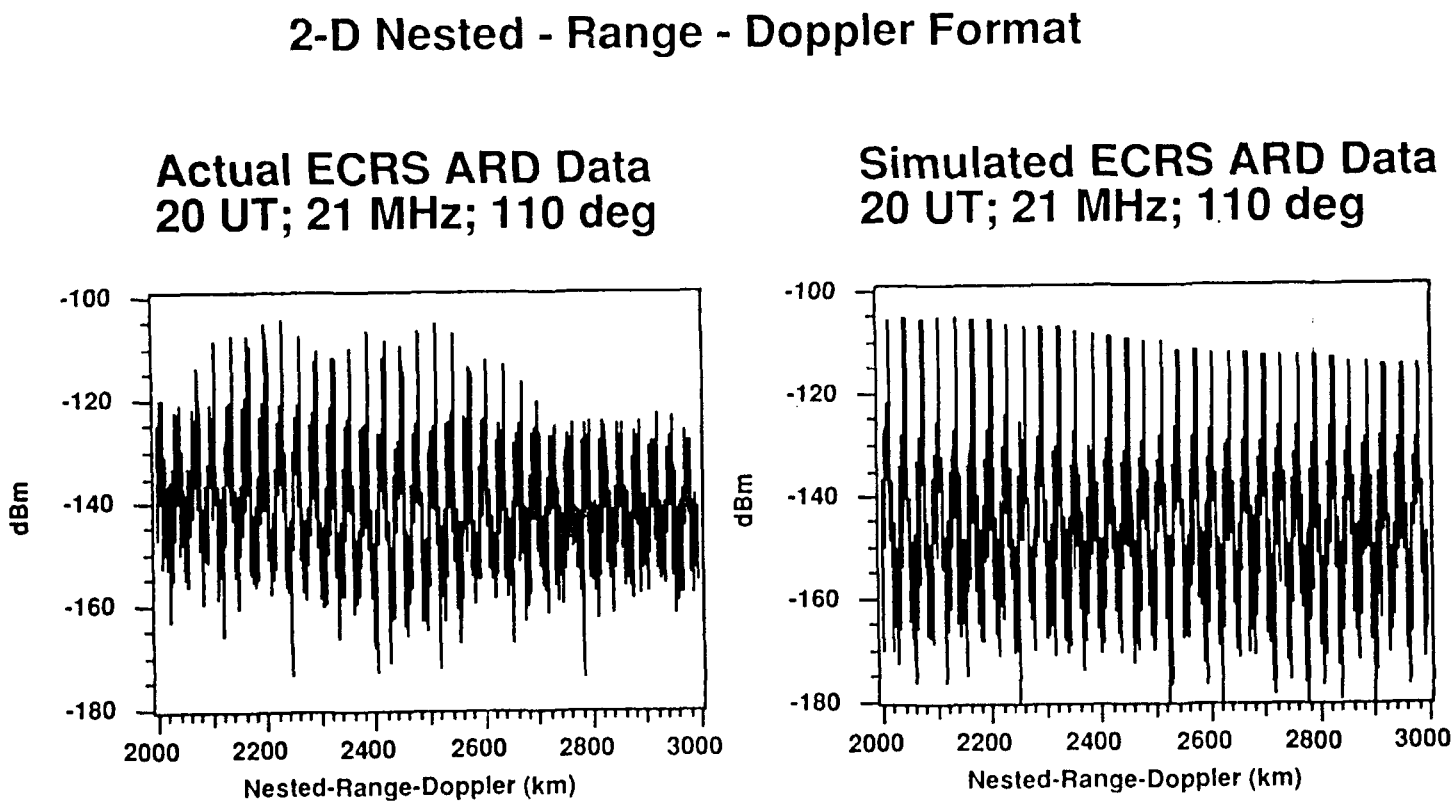

Figure 11. Measured and Simulated Equatorial Range-Folded Clutter

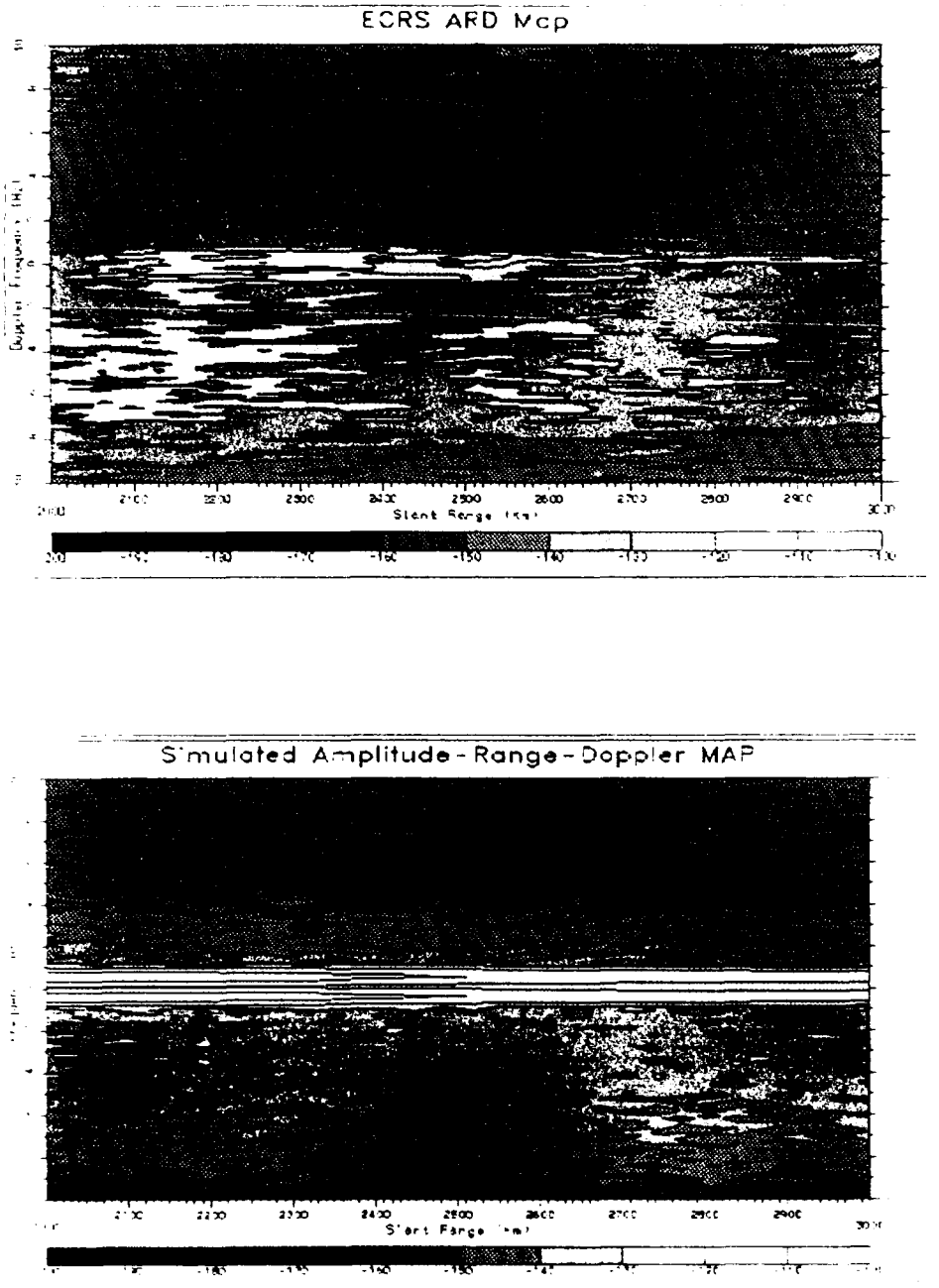

Figure 12. Measured and Simulated Equatorial Range-Folded Clutter ARD Maps

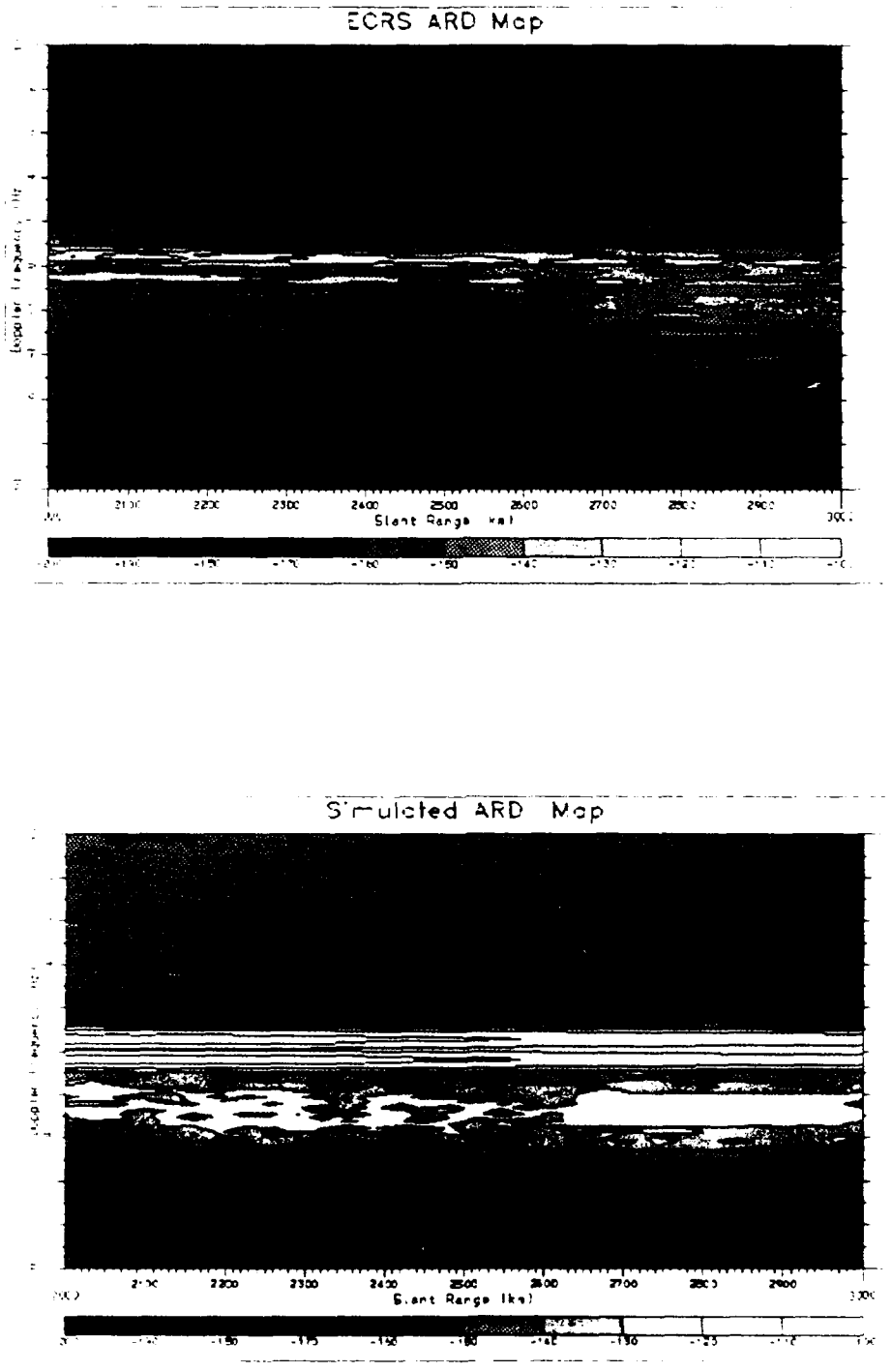

Figure 13. Measured and Simulated Equatorial Range-Folded Clutter ARD Maps for an Azimuth of 140 Degrees

DISTRIBUTION LIST

INTERNAL

A010

R. D. Haggarty
E. L. Key

A030

R. L. Fante
R. W. Jacobus

D010

E. J. Ferrari

D011

B. A. Deresh
W. I. Fenster

D050

J. W. Betz
E. A. Palo
B. D. Perry

D051

Y. Avniel
S. Dhar
S. D. O'Neil
R. Rifkin
R. P. Perry
S. A. Townes

D080

R. Wm. Bush
R. M. Davis
C. H. Gager
A. J. Goldberg
G. L. Guttrich
J. D. R. Kramer, Jr.
E. D. Ostroff

D080 (Concl'd)

J. Providakes (10)
G. W. Randig
J. M. Schoen
W. E. Sievers

D081

N. F. Doherty
J. E. Levy
R. C. Smith
A. L. Snyder
R. B. Young

D085

R. M. Coutts
L. M. DeRoeck
R. B. Godwin
S. N. Hunt
K. T. Kim
J. E. Kriegel
P. T. Lee
T. S. Lee
D. C. Miller
J. B. Moran
J. D. Moylan
K. R. Overfield
J. L. Pearlman
G. A. Robertshaw
K. B. Sarachik
J. C. Tang
L. J. Teig
N. M. Tomljanovich
L. D. Tromp
D. J. Violette
M. M. Weiner

D090

P. A. Bello

amplitude-range-Doppler (ARD) data at a radar azimuth of 140 degrees . The agreement shown in figure 13 is not as good as that shown in figure 12; however, the spectral shape is similar. The simulated ARD map shows the equatorial clutter with a Doppler shift larger than that of the measured data. However, this disagreement is easily encompassed within the day-to-day and longitudinal variability of equatorial vertical drifts. The most important feature to note is the fact that both the simulated and measured clutter data decreases in Doppler spreading and Doppler shift are evident at the azimuth of 140 degrees as compared to 110 degrees. This is consistent with the intensity distribution of equatorial spread F, which is a strong function of local time after E-region sunset. Since the local time at the 140-degree equatorial point is earlier than the 110-degree equatorial point, we should expect to observe less Doppler spread and smaller Doppler shifts in the 140-degree azimuth beam, which is consistent with the simulation results.

Another important property of the simulation is the ability to turn off or turn on various features in the geophysics in much the same manner that nature does, thereby allowing us to improve our understanding of the day-to-day variability of OTH clutter. In future studies we hope to make further comparisons between the simulation and measurement of OTH radar clutter data under various geophysical conditions. We may also generate simulated time-series data of clutter as well as targets and other HF sources; this would, for example, allow various clutter mitigation schemes or detection and tracking techniques to be evaluated entirely with the simulation, without the need for real radar data.